

These semaphorins form a family of immunoregulatory molecules, called 'immune semaphorins'. Lack of semaphorin family proteins results in several immune disorders, including autoimmune diseases, allergy, and congenital bone disease. Alternatively, lack of these proteins induces unresponsiveness to physiological immune responses. Therefore, semaphorin family proteins are at least responsible for the maintenance of immunological homeostasis, based on the sophisticated immune cell communication system. However, several important issues remain to be resolved. Although semaphorins function to regulate cell motility and morphology by activating plexins, most of the immunological studies of semaphorins have only focused on their costimulatory effects. Several functional receptors other than plexins have been identified in the immune system; however, it still remains a possibility that semaphorins exert their functions by affecting cell cytoskeleton. In addition, several lines of evidence indicate that transmembrane semaphorins serve not only as ligands but also as receptors, a process termed bidirectional signaling. This semaphorin-mediated backward signaling may also influence immune cell reactions. Further studies are required to clarify the role of semaphorins in immune cell morphology and dynamics. Finally, understanding of the immune semaphorins should allow pharmacological modulation of their functions leading to potential therapeutic targets for several immune diseases.

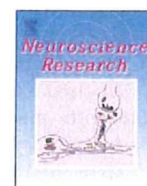
Acknowledgments We thank K. Kubota for secretarial assistance. This study was supported by the Core Research for Evolutional Science and Technology program of the Japanese Science and Technology Agency and Grant-in-Aid for Scientific Research (S)-20229007 of the Japan Society for the Promotion of Science.

References

- Steinman L. Elaborate interactions between the immune and nervous systems. *Nat Immunol.* 2004;5:575–81. doi:10.1038/nri1078.
- Kolodkin AL, Matthes DJ, Goodman CS. The semaphorin genes encode a family of transmembrane and secreted growth cone guidance molecules. *Cell* 1993;75:1389–99. doi:10.1016/0092-8674(93)90625-Z.
- Semaphorin Nomenclature Committee. Unified nomenclature for the semaphorins/collapsins. *Cell* 1999;97:551–2. doi:10.1016/S0092-8674(00)80766-7.
- Zhou Y, Gumpert RA, Pasterkamp RJ. Semaphorin signaling: progress made and promises ahead. *Trends Biochem Sci.* 2008; 33:161–70. doi:10.1016/j.tibs.2008.01.006.
- Tamagnone L, Artigiani S, Chen H, He Z, Ming GI, Song H, et al. Plexins are a large family of receptors for transmembrane, secreted, and GPI-anchored semaphorins in vertebrates. *Cell* 1999;99:71–80. doi:10.1016/S0092-8674(00)80063-X.
- Winberg ML, Noordermeer JN, Tamagnone L, Comoglio PM, Spriggs MK, Tessier-Lavigne M, et al. Plexin A is a neuronal semaphorin receptor that controls axon guidance. *Cell* 1998; 95:903–16. doi:10.1016/S0092-8674(00)81715-8.
- Kruger RP, Aurandt J, Guan KL. Semaphorins command cells to move. *Nat Rev Mol Cell Biol.* 2005;6:789–800. doi:10.1038/nrm1740.
- Takahashi T, Fournier A, Nakamura F, Wang LH, Murakami Y, Kalb RG, et al. Plexin-neuropilin-1 complexes form functional semaphorin-3A receptors. *Cell* 1999;99:59–69. doi:10.1016/S0092-8674(00)80062-8.
- Toyofuku T, Kikutani H. Semaphorin signaling during cardiac development. *Adv Exp Med Biol.* 2007;600:109–17. doi:10.1007/978-0-387-70956-7_9.
- Geretti E, Shimizu A, Klagsbrun M. Neuropilin structure governs VEGF and semaphorin binding and regulates angiogenesis. *Angiogenesis* 2008;11:31–9. doi:10.1007/s10456-008-9097-1.
- Toyofuku T, Yabuki M, Kamei J, Kamei M, Makino N, Kumanogoh A, et al. Semaphorin-4A, an activator for T-cell-mediated immunity, suppresses angiogenesis via Plexin-D1. *EMBO J.* 2007;26:1373–84. doi:10.1038/sj.emboj.7601589.
- Casazza A, Fazzari P, Tamagnone L. Semaphorin signals in cell adhesion and cell migration: functional role and molecular mechanisms. *Adv Exp Med Biol.* 2007;600:90–108. doi:10.1007/978-0-387-70956-7_8.
- Giordano S, Corso S, Conrotto P, Artigiani S, Gilestro G, Barberis D, et al. The semaphorin 4D receptor controls invasive growth by coupling with Met. *Nat Cell Biol.* 2002;4:720–4. doi:10.1038/ncb843.
- Bielenberg DR, Klagsbrun M. Targeting endothelial and tumor cells with semaphorins. *Cancer Metastasis Rev.* 2007;26:421–31. doi:10.1007/s10555-007-9097-4.
- Suzuki K, Kumanogoh A, Kikutani H. Semaphorins and their receptors in immune cell interactions. *Nat Immunol.* 2008;9:17–23. doi:10.1038/nri1553.
- Kikutani H, Suzuki K, Kumanogoh A. Immune semaphorins: increasing members and their diverse roles. *Adv Immunol.* 2007;93:121–43. doi:10.1016/S0065-2776(06)93003-X.
- Kikutani H, Kumanogoh A. Semaphorins in interactions between T cells and antigen-presenting cells. *Nat Rev Immunol.* 2003;3:159–67. doi:10.1038/nri1003.
- Toyofuku T, Zhang H, Kumanogoh A, Takegahara N, Suto F, Kamei J, et al. Dual roles of Sema6D in cardiac morphogenesis through region-specific association of its receptor, Plexin-A1, with off-track and vascular endothelial growth factor receptor type 2. *Genes Dev.* 2004;18:435–47. doi:10.1101/gad.1167304.
- Kumanogoh A, Watanabe C, Lee I, Wang X, Shi W, Araki H, et al. Identification of CD72 as a lymphocyte receptor for the class IV semaphorin CD100: a novel mechanism for regulating B cell signaling. *Immunity* 2000;13:621–31. doi:10.1016/S1074-7613(00)00062-5.
- Kumanogoh A, Marukawa S, Suzuki K, Takegahara N, Watanabe C, Cheng E, et al. Class IV semaphorin Sema4A enhances T-cell activation and interacts with Tim-2. *Nature* 2002;419:629–33. doi:10.1038/nature01037.
- Hall KT, Bousmell L, Schultze JL, Bousiotis VA, Dorfman DM, Cardoso AA, et al. Human CD100, a novel leukocyte semaphorin that promotes B-cell aggregation and differentiation. *Proc Natl Acad Sci USA.* 1996;93:11780–5. doi:10.1073/pnas.93.21.11780.
- Furuyama T, Inagaki S, Kosugi A, Noda S, Saitoh S, Ogata M, et al. Identification of a novel transmembrane semaphorin expressed on lymphocytes. *J Biol Chem.* 1996;271:33376–81. doi:10.1074/jbc.271.52.33376.
- Dorfman DM, Shahsafaei A, Nadler LM, Freeman GJ. The leukocyte semaphorin CD100 is expressed in most T-cell, but few B-cell, non-Hodgkin's lymphomas. *Am J Pathol.* 1998;153:255–62.
- Delaire S, Elhabazi A, Bensussan A, Bousmell L. CD100 is a leukocyte semaphorin. *Cell Mol Life Sci.* 1998;54:1265–76. doi:10.1007/s000180050252.

25. Shi W, Kumanogoh A, Watanabe C, Uchida J, Wang X, Yasui T, et al. The class IV semaphorin CD100 plays nonredundant roles in the immune system: defective B and T cell activation in CD100-deficient mice. *Immunity* 2000;13:633–42. doi:10.1016/S1074-7613(00)00063-7.
26. Oinuma I, Ishikawa Y, Katoh H, Negishi M. The semaphorin 4D receptor Plexin-B1 is a GTPase activating protein for R-Ras. *Science* 2004;305:862–5. doi:10.1126/science.1097545.
27. Adachi T, Flaswinkel H, Yakura H, Reth M, Tsubata T. The B cell surface protein CD72 recruits the tyrosine phosphatase SHP-1 upon tyrosine phosphorylation. *J Immunol*. 1998;160:4662–5.
28. Parnes JR, Pan C. CD72, a negative regulator of B-cell responsiveness. *Immunol Rev*. 2000;176:75–85. doi:10.1034/j.1600-065X.2000.00608.x.
29. Pan C, Baumgarth N, Parnes JR. CD72-deficient mice reveal nonredundant roles of CD72 in B cell development and activation. *Immunity* 1999;11:495–506. doi:10.1016/S1074-7613(00)80124-7.
30. Kumanogoh A, Kikutani H. The CD100-CD72 interaction: a novel mechanism of immune regulation. *Trends Immunol*. 2001;22:670–6. doi:10.1016/S1471-4906(01)02087-7.
31. Niiro H, Clark EA. Regulation of B-cell fate by antigen-receptor signals. *Nat Rev Immunol*. 2002;2:945–56. doi:10.1038/nri955.
32. Kumanogoh A, Shikina T, Watanabe C, Takegahara N, Suzuki K, Yamamoto M, et al. Requirement for CD100-CD72 interactions in fine-tuning of B-cell antigen receptor signaling and homeostatic maintenance of the B-cell compartment. *Int Immunol*. 2005;17:1277–82. doi:10.1093/intimm/dxh307.
33. Samardzic T, Marinkovic D, Danzer CP, Gerlach J, Nitschke L, Wirth T. Reduction of marginal zone B cells in CD22-deficient mice. *Eur J Immunol*. 2002;32:561–7. doi:10.1002/1521-4141(200202)32:2<561::AID-IMMU561>3.0.CO;2-H.
34. Lopes-Carvalho T, Kearney JF. Development and selection of marginal zone B cells. *Immunol Rev*. 2004;197:192–205. doi:10.1111/j.0105-2896.2004.0112.x.
35. Li DH, Winslow MM, Cao TM, Chen AH, Davis CR, Mellins ED, et al. Modulation of peripheral B cell tolerance by CD72 in a murine model. *Arthritis Rheum*. 2008;58:3192–204. doi:10.1002/art.23812.
36. Ishida I, Kumanogoh A, Suzuki K, Akahani S, Noda K, Kikutani H. Involvement of CD100, a lymphocyte semaphorin, in the activation of the human immune system via CD72: implications for the regulation of immune and inflammatory responses. *Int Immunol*. 2003;15:1027–34. doi:10.1093/intimm/dxg098.
37. Kumanogoh A, Suzuki K, Ch'ng E, Watanabe C, Marukawa S, Takegahara N, et al. Requirement for the lymphocyte semaphorin, CD100, in the induction of antigen-specific T cells and the maturation of dendritic cells. *J Immunol*. 2002;169:1175–81.
38. Li M, O'Sullivan KM, Jones LK, Semple T, Kumanogoh A, Kikutani H, et al. CD100 enhances dendritic cell and CD4+ cell activation leading to pathogenetic humoral responses and immune complex glomerulonephritis. *J Immunol*. 2006;177:3406–12.
39. Wang X, Kumanogoh A, Watanabe C, Shi W, Yoshida K, Kikutani H. Functional soluble CD100/Sema4D released from activated lymphocytes: possible role in normal and pathologic immune responses. *Blood* 2001;97:3498–504. doi:10.1182/blood.V97.11.3498.
40. Watanabe C, Kumanogoh A, Shi W, Suzuki K, Yamada S, Okabe M, et al. Enhanced immune responses in transgenic mice expressing a truncated form of the lymphocyte semaphorin CD100. *J Immunol*. 2001;167:4321–8.
41. Giraudon P, Vincent P, Vuaillet C, Verlaeten O, Cartier L, Marie-Cardine A, et al. Semaphorin CD100 from activated T lymphocytes induces process extension collapse in oligodendrocytes and death of immature neural cells. *J Immunol*. 2004;172:1246–55.
42. Kumanogoh A, Shikina T, Suzuki K, Uematsu S, Yukawa K, Kashiwamura S, et al. Nonredundant roles of Sema4A in the immune system: defective T cell priming and Th1/Th2 regulation in Sema4A-deficient mice. *Immunity* 2005;22:305–16. doi:10.1016/j.immuni.2005.01.014.
43. Rice DS, Huang W, Jones HA, Hansen G, Ye GL, Xu N, et al. Severe retinal degeneration associated with disruption of semaphorin 4A. *Invest Ophthalmol Vis Sci*. 2004;45:2767–77. doi:10.1167/iov.04-0020.
44. McIntire JJ, Umetsu SE, Akbari O, Potter M, Kuchroo VK, Barsh GS, et al. Identification of Tapr (an airway hyperreactivity regulatory locus) and the linked Tim gene family. *Nat Immunol*. 2001;2:1109–16. doi:10.1038/nri739.
45. Kuchroo VK, Dardalhon V, Xiao S, Anderson AC. New roles for TIM family members in immune regulation. *Nat Rev Immunol*. 2008;8:577–80. doi:10.1038/nri2366.
46. Meyers JH, Sabatos CA, Chakravarti S, Kuchroo VK. The TIM gene family regulates autoimmune and allergic diseases. *Trends Mol Med*. 2005;11:362–9. doi:10.1016/j.molmed.2005.06.008.
47. Mizui M, Shikina T, Arase H, Suzuki K, Yasui T, Rennert PD, et al. Bimodal regulation of T cell-mediated immune responses by TIM-4. *Int Immunol*. 2008;20:695–708. doi:10.1093/intimm/dxn029.
48. Kuchroo VK, Umetsu DT, DeKruyff RH, Freeman GJ. The TIM gene family: emerging roles in immunity and disease. *Nat Rev Immunol*. 2003;3:454–62. doi:10.1038/nri1111.
49. Chakravarti S, Sabatos CA, Xiao S, Illes Z, Cha EK, Sobel RA, et al. Tim-2 regulates T helper type 2 responses and autoimmunity. *J Exp Med*. 2005;202:437–44. doi:10.1084/jem.20050308.
50. Rennert PD, Ichimura T, Sizing ID, Bailly V, Li Z, Rennard R, et al. T cell, Ig domain, mucin domain-2 gene-deficient mice reveal a novel mechanism for the regulation of Th2 immune responses and airway inflammation. *J Immunol*. 2006;177:4311–21.
51. Yamada A, Kubo K, Takeshita T, Harashima N, Kawano K, Mine T, et al. Molecular cloning of a glycosylphosphatidylinositol-anchored molecule CDw108. *J Immunol*. 1999;162:4094–100.
52. Mine T, Harada K, Matsumoto T, Yamana H, Shirouzu K, Itoh K, et al. CDw108 expression during T-cell development. *Tissue Antigens*. 2000;55:429–36. doi:10.1034/j.1399-0039.2000.550505.x.
53. Tamagnone L, Comoglio PM. Signalling by semaphorin receptors: cell guidance and beyond. *Trends Cell Biol*. 2000;10:377–83. doi:10.1016/S0962-8924(00)01816-X.
54. Scott GA, McClelland LA, Fricke AF. Semaphorin 7a promotes spreading and dendricity in human melanocytes through beta1-integrins. *J Invest Dermatol*. 2008;128:151–61. doi:10.1038/sj.jid.5700974.
55. Pasterkamp RJ, Peschon JJ, Spriggs MK, Kolodkin AL. Semaphorin 7A promotes axon outgrowth through integrins and MAPKs. *Nature* 2003;424:398–405. doi:10.1038/nature01790.
56. Suzuki K, Okuno T, Yamamoto M, Pasterkamp RJ, Takegahara N, Takamatsu H, et al. Semaphorin 7A initiates T-cell-mediated inflammatory responses through alpha1beta1 integrin. *Nature* 2007;446:680–4. doi:10.1038/nature05652.
57. Holmes S, Downs AM, Fosberry A, Hayes PD, Michalovich D, Murdoch P, et al. Sema7A is a potent monocyte stimulator. *Scand J Immunol*. 2002;56:270–5. doi:10.1046/j.1365-3083.2002.01129.x.
58. Alderson MR, Armitage RJ, Tough TW, Strockbine L, Fanslow WC, Spriggs MK. CD40 expression by human monocytes: regulation by cytokines and activation of monocytes by the ligand for CD40. *J Exp Med*. 1993;178:669–74. doi:10.1084/jem.178.2.669.
59. Toyofuku T, Zhang H, Kumanogoh A, Takegahara N, Yabuki M, Harada K, et al. Guidance of myocardial patterning in cardiac development by Sema6D reverse signalling. *Nat Cell Biol*. 2004;6:1204–11. doi:10.1038/ncb1193.
60. Wong AW, Brickey WJ, Taxman DJ, van Deventer HW, Reed W, Gao JX, et al. CITA-regulated plexin-A1 affects T-cell-dendritic cell interactions. *Nat Immunol*. 2003;4:891–8. doi:10.1038/nri960.

61. Takegahara N, Takamatsu H, Toyofuku T, Tsujimura T, Okuno T, Yukawa K, et al. Plexin-A1 and its interaction with DAP12 in immune responses and bone homeostasis. *Nat Cell Biol.* 2006;8:615–22. doi:10.1038/ncb1416.
62. Tomasello E, Desmoulins PO, Chemin K, Guia S, Cremer H, Ortaldo J, et al. Combined natural killer cell and dendritic cell functional deficiency in KARAP/DAP12 loss-of-function mutant mice. *Immunity* 2000;13:355–64. doi:10.1016/S1074-7613(00)00035-2.
63. Zompi S, Hamerman JA, Ogasawara K, Schweighoffer E, Tybulewicz VL, Di Santo JP, et al. NKG2D triggers cytotoxicity in mouse NK cells lacking DAP12 or Syk family kinases. *Nat Immunol.* 2003;4:565–72. doi:10.1038/ni930.
64. Bakker AB, Hoek RM, Cerwenka A, Blom B, Lucian L, McNeil T, et al. DAP12-deficient mice fail to develop autoimmunity due to impaired antigen priming. *Immunity* 2000;13:345–53. doi:10.1016/S1074-7613(00)00034-0.
65. Kaifu T, Nakahara J, Inui M, Mishima K, Momiyama T, Kaji M, et al. Osteopetrosis and thalamic hypomyelination with synaptic degeneration in DAP12-deficient mice. *J Clin Invest.* 2003; 111:323–32.
66. O'Connor BP, Eun SY, Ye Z, Zozulya AL, Lich JD, Moore CB, et al. Semaphorin 6D regulates the late phase of CD4+ T cell primary immune responses. *Proc Natl Acad Sci USA.* 2008; 105:13015–20. doi:10.1073/pnas.0803386105.
67. Comeau MR, Johnson R, DuBose RF, Petersen M, Gearing P, VandenBos T, et al. A poxvirus-encoded semaphorin induces cytokine production from monocytes and binds to a novel cellular semaphorin receptor, VESPR. *Immunity* 1998;8:473–82. doi:10.1016/S1074-7613(00)80552-X.
68. Walzer T, Galibert L, Comeau MR, De Smedt T. Plexin C1 engagement on mouse dendritic cells by viral semaphorin A39R induces actin cytoskeleton rearrangement and inhibits integrin-mediated adhesion and chemokine-induced migration. *J Immunol.* 2005;174:51–9.
69. Walzer T, Galibert L, De Smedt T. Poxvirus semaphorin A39R inhibits phagocytosis by dendritic cells and neutrophils. *Eur J Immunol.* 2005;35:391–8. doi:10.1002/eji.200425669.
70. Lepelletier Y, Moura IC, Hadj-Slimane R, Renand A, Fiorentino S, Baude C, et al. Immunosuppressive role of semaphorin-3A on T cell proliferation is mediated by inhibition of actin cytoskeleton reorganization. *Eur J Immunol.* 2006;36:1782–93. doi:10.1002/eji.200535601.
71. Moretti S, Procopio A, Lazzarini R, Rippon MR, Testa R, Marra M, et al. Semaphorin3A signaling controls Fas (CD95)-mediated apoptosis by promoting Fas translocation into lipid rafts. *Blood* 2008;111:2290–9. doi:10.1182/blood-2007-06-096529.
72. Yamamoto M, Suzuki K, Okuno T, Ogata T, Takegahara N, Takamatsu H, et al. Plexin-A4 negatively regulates T lymphocyte responses. *Int Immunol.* 2008;20:413–20. doi:10.1093/intimm/dxn006.
73. Suto F, Tsuboi M, Kamiya H, Mizuno H, Kiyama Y, Komai S, et al. Interactions between plexin-A2, plexin-A4, and semaphorin 6A control lamina-restricted projection of hippocampal mossy fibers. *Neuron* 2007;53:535–47. doi:10.1016/j.neuron.2007.01.028.
74. Tordjiman R, Lepelletier Y, Lemarchandel V, Cambot M, Gaulard P, Hermine O, et al. A neuronal receptor, neuropilin-1, is essential for the initiation of the primary immune response. *Nat Immunol.* 2002;3:477–82.
75. Bruder D, Probst-Kepper M, Westendorf AM, Geffers R, Beissert S, Loser K, et al. Neuropilin-1: a surface marker of regulatory T cells. *Eur J Immunol.* 2004;34:623–30. doi:10.1002/eji.200324799.
76. Hill JA, Feuerer M, Tash K, Haxhinasto S, Perez J, Melamed R, et al. Foxp3 transcription-factor-dependent and -independent regulation of the regulatory T cell transcriptional signature. *Immunity* 2007;27:786–800.
77. Sarris M, Andersen KG, Randow F, Mayr L, Betz AG. Neuropilin-1 expression on regulatory T cells enhances their interactions with dendritic cells during antigen recognition. *Immunity* 2008;28:402–13. doi:10.1016/j.immuni.2008.01.012.
78. Delaire S, Billard C, Tordjiman R, Chedotal A, Elhabazi A, Bensussan A, et al. Biological activity of soluble CD100. II. Soluble CD100, similarly to H-SemaIII, inhibits immune cell migration. *J Immunol.* 2001;166:4348–54.
79. Zhu L, Bergmeier W, Wu J, Jiang H, Stalker TJ, Cieslak M, et al. Regulated surface expression and shedding support a dual role for semaphorin 4D in platelet responses to vascular injury. *Proc Natl Acad Sci USA.* 2007;104:1621–6. doi:10.1073/pnas.0606344104.
80. Mizrahi S, Markel G, Porgador A, Bushkin Y, Mandelboim O. CD100 on NK cells enhance IFN γ secretion and killing of target cells expressing CD72. *PLoS One.* 2007;2:e818. doi:10.1371/journal.pone.0000818.



Membrane potential response profiles of CA1 pyramidal cells probed with voltage-sensitive dye optical imaging in rat hippocampal slices reveal the impact of GABA_A-mediated feed-forward inhibition in signal propagation

Yoko Tominaga^{a,c}, Michinori Ichikawa^{c,1}, Takashi Tominaga^{a,b,c,*}

^a Department of Neurophysiology, Kagawa School of Pharmaceutical Sciences, Tokushima Bunri University, 1314-1 Shido, Sanuki, Kagawa 769-2193, Japan

^b Laboratory for Dynamics of Emergent Intelligence, RIKEN Brain Science Institute (BSI), 2-1 Hirosawa, Wako, Saitama 351-0198, Japan

^c Laboratory for Brain-Operative Devices, RIKEN Brain Science Institute (BSI), 2-1 Hirosawa, Wako, Saitama 351-0198, Japan

ARTICLE INFO

Article history:

Received 30 April 2008

Received in revised form 17 February 2009

Accepted 19 February 2009

Available online 5 March 2009

Keywords:

Dendrite

Integration

Action potential firing

Computer simulation

ABSTRACT

The spatial and temporal distribution of excitatory and inhibitory membrane potential responses on a cell plays an important role in neuronal calculations in local neuronal circuits in the brain. The electrical dynamics of excitatory and inhibitory inputs along the somatodendritic extent of CA1 pyramidal cells during circuit activation were examined by stimulating strata radiatum (SR), oriens (SO), and lacunosum-moleculare (SLM) and measuring laminar responses with voltage-sensitive dye (VSD) optical recording methods. We first confirmed the linearity of the optical signal by comparing fluorescence changes in CA1 to global membrane potential changes when slices were bathed in high-potassium ($[K^+]_o = 25$ mM) solution. Except for a TTX-sensitive component in stratum pyramidale, fluorescence changes were equal in all strata, indicating that VSD sensitivity had reasonable linearity across layers. We then compared membrane potential profiles in slices exposed to picrotoxin, a GABA_A receptor antagonist. We attributed the picrotoxin-induced changes in the first peak of the excitatory membrane potential to feed-forward inhibition and the later response (appearing 30 ms after stimulation) to feedback inhibition. A difference in feed-forward components was observed in perisomatic and distal apical dendritic regions after SR stimulation. SLM stimulation produced large differences in perisomatic and apical dendritic regions. SO stimulation, however, produced no feed-forward inhibition at the perisomatic region, but produces feed-forward inhibition in distal dendritic regions. These results suggest that actual inhibition of membrane potential response by feed-forward inhibition is greater at perisomatic regions after SR or SLM stimulation but is smaller at distal dendritic regions after SR, SO, and SLM stimulation.

© 2009 Elsevier Ireland Ltd and the Japan Neuroscience Society. All rights reserved.

1. Introduction

Neurons possess highly organized membrane structures through which membrane potential fluctuations play an important role in the integration of neural information. The integration properties of a neuron largely depend on neuronal channel properties and geometries. Many electrophysiological methods can directly access the electrical properties of dendrites (Stuart et al., 1993; Davie et al., 2006), even those of fine basal dendrites (Nevian et al., 2007). However, the actual degree of activation of

excitatory and especially of inhibitory synapses terminating on a cell in on-going neuronal circuit activity is not clear.

The existence of inhibitory postsynaptic potentials elicited by stimulating the main input to the CA1 circuit has been long known (Kandel et al., 1961; Andersen et al., 1963, 1964; Buzsaki, 1984). This circuit has been designated as a recurrent inhibitory system. Feed-forward inhibition activated by orthodromic stimulation has also been identified (Dingledine and Gjerstad, 1980; Alger and Nicoll, 1982b). The locus of inhibitory synaptic input has been tested by local application of GABA in combination with local electrical stimulation (Andersen et al., 1980; Alger and Nicoll, 1982a), and the time course of the inhibitory input has been shown to overlap with the excitatory input (Dingledine and Langmoen, 1980; Brown and Johnston, 1983; Griffith et al., 1986; Turner, 1990; Karnup and Stelzer, 1999). Inhibition largely depends on shunting control and scarcely appears in the membrane potential trace (Turner, 1988; Sayer et al., 1989; Pouille and Scanziani, 2004). Thus, it has been difficult to measure the impact of inhibitory input

* Corresponding author at: Kagawa School of Pharmaceutical Sciences, Tokushima Bunri University, 1314-1 Shido, Sanuki, Kagawa 769-2193, Japan. Tel.: +81 87 894 5111x6708; fax: +81 87 894 0181.

E-mail address: tominagat@kph.bunri-u.ac.jp (T. Tominaga).

¹ Present address: BrainVision Inc., 3-46-8 Narimasu, Itabashi, Tokyo 175-0094, Japan.

on the membrane potential response, especially in terms of its distribution along the somatodendritic axis of a cell. Since optical recording methods can visualize population behaviors within the CA1 circuit, we used this method to map the distribution of GABA_A receptor-mediated inhibition along the somatodendritic axis of CA1 pyramidal cells (Megias et al., 2001) and to determine to what extent inhibition contributes to CA1 signal transduction.

The optical imaging method with voltage-sensitive dyes (VSDs) represents a potentially useful tool for examining integration processes (e.g., Antic and Zecevic, 1995; Antic, 2003). Because of its simple lamellar organization (Andersen et al., 1969b), the *in vitro* hippocampal slice preparation is ideal for studying neural integration in neural circuits. Optical imaging with VSDs has many advantages (Grinvald et al., 1982; Barish et al., 1996; Tominaga et al., 2000, 2001, 2002; Inoue et al., 2001; Mochida et al., 2001; Aihara et al., 2005; Mann et al., 2005a; Chang and Jackson, 2006): It allows direct viewing of hippocampal layers, thus allowing optical signals to be attributed to specific membrane areas of the major cell type, the pyramidal cell. For example, neural integration in area CA1 can be assessed by examining signals in stratum radiatum (SR), which correspond primarily to the membrane potential responses of pyramidal cell apical dendrites, and signals in stratum pyramidale (SP), which correspond primarily to membrane potential responses of pyramidal cell somas.

One potential drawback of optical recording, however, is that the nature of optical signals precludes an interpretation of the optical data in terms of absolute membrane potentials. A typical example is seen in optical signals resulting from stimulation of Schaffer collateral axons in SR. Even if the stimulus intensity is high enough to obtain saturated population spikes, the optical signals measured from SR (which correspond to a few tens of millivolts of excitatory postsynaptic potential [EPSP]), are larger than those measured from SP (which correspond to over a hundred millivolts of action potential). To identify the potential source of this disparity, we analyzed steady membrane potential changes in slices perfused with high-potassium medium, and examined the profiles of population membrane potential responses using a simulator called NEURON (Hines and Carnevale, 1997). The results suggest that the nature of the population optical signal is the major cause of the disparity.

Taking advantage of this optical measurement method, we have successfully characterized the inhibitory action and its distribution on actual membrane potential response of feed-forward and feedback inhibition within Schaffer collateral inputs to the perisomatic region of CA1 pyramidal cells and found that the spatial contribution of inhibitory inputs onto postsynaptic cells differed.

Some preliminary results of this study have been published in abstract form (Tominaga et al., 2003).

2. Materials and methods

All animal experiments were performed according to protocols approved by the Animal Care and Use Committee of Tokushima Bunri University and RIKEN, and the U.S. National Institutes of Health Guide for the Care and Use of Laboratory Animals. All efforts were made to minimize the number of animals used and their suffering.

2.1. Slice preparation and staining with VSD

Hippocampal slices (400 μ m thick) were prepared from 4- to 5-week-old male rats, decapitated under deep-ether anesthesia. The brains were quickly cooled in ice-cold artificial cerebrospinal fluid (aCSF) (124 mM NaCl, 2.5 mM KCl, 2 mM CaCl₂, 2 mM MgSO₄,

1.25 mM NaH₂PO₄, 26 mM NaHCO₃, and 10 mM glucose, pH 7.4) bubbled with 95%/5% O₂/CO₂ gas. After cooling for 5 min, the hippocampus was dissected out along with the surrounding cortex and sliced into 400- μ m-thick transverse sections with a vibratome (Leica VT-1000). Following a short incubation in gassed aCSF for 3–5 min, each slice was transferred onto a fine-mesh membrane filter (Omni Pore membrane filter, JHWP01300; Millipore Corp., MA, USA), held in place by a thin Plexiglas ring (inner diameter, 11 mm; outer diameter, 15 mm; thickness 1–2 mm). These slices were transferred to a moist chamber continuously supplied with the humidified O₂ and CO₂ gas mixture. The temperature was held at 32 °C for 1 h, and then maintained at room temperature. After 1 h of incubation, slices were stained with VSD (100 μ l of staining solution/slice) for 25 min and washed with normal aCSF. VSD (0.2 mM Di-4-ANEPPS; D-1199, Molecular Probes Inc., OR, USA) was dissolved in a mixture of 2.7% ethanol, 0.13% Cremophor EL (Sigma), 50% fetal bovine serum (Sigma), and 50% aCSF. The slices were subjected to experiments after at least 1 h incubation at room temperature after the wash.

2.2. Optical recording

The Plexiglas ring supporting an individual slice was placed in an immersion-type recording chamber. Slices were continuously perfused with prewarmed (31 °C) and oxygenated (95%/5% O₂/CO₂ gas mixture) aCSF at a rate of 1 ml/min. Custom laboratory-designed epifluorescence optics consisting of two principal lenses was used. The optics consisting of a modified 35-mm camera lens ($f = 50$ mm F/1.4, Nikon; the final magnification of the system was $\times 1.5$) or a custom made objective lens (Olympus MYCAM 5 \times /0.6 W); the final magnification of the system was about $\times 5$) as the objective lens, and a lens ($f = 55$ mm \times 1.0 Leica Microsystems MZ-APO) as the projection lens. The excitation light was provided by a halogen lamp source (150 W; MHW-G150LR, Moritex Corp.) through an excitation filter ($\lambda = 530 \pm 10$ nm) and reflected onto a specimen by a dichroic mirror ($\lambda = 575$ nm). Fluorescence was passed through an emission filter ($\lambda > 590$ nm) and projected onto a CCD camera or a MOS imager (MiCAM01 and MiCAM Ultima, respectively; BrainVision, Inc., Tokyo, Japan). Optical signals were calculated as the ratio of fractional change in VSD fluorescence to baseline VSD fluorescence ($\Delta F/F$). The optical signals referred to in the following sections represent signals filtered in spatial and temporal dimensions with a Gaussian kernel of $5 \times 5 \times 3$ (horizontal \times vertical \times temporal). We confirmed that this procedure produced steady and flat baselines and did not cause any artificial drift in signals in the absence of electrical stimulation. We analyzed the optical signals offline using a procedure developed for Igor Pro (WaveMetrics Inc., OR, USA). VSD fluorescence at a wavelength of 530 nm decreases in response to the depolarization of the membrane. To fit the polarity of the response to conventional membrane potential changes, we expressed the optical signal in a polarity that matches the membrane potential change. For example, decreased fluorescence, which corresponds to depolarization, is represented as a positive deflection. However, when a global fluorescence change was observed, we used the polarity of the fluorescence change, as shown in Fig. 2.

2.3. Time-lapse imaging

Since the imaging system was created and optimized for fast acquisition, slow changes in fluorescence, such as responses to bath application of test solutions, could not be evaluated. Accumulation of static charges on pixels of the imager over long periods tended to create unstable drifts in the baseline. To mitigate this problem, we acquired 85 consecutive frames of data at short intervals (85 frames at rate of 1 ms/frame), every 10 s. The

consecutive images captured during each frame were averaged, and this average represented frame data for each 10 s interval. A sequence of frames was produced using a macro developed for use in the MiCAM01 image acquisition program. These sequences were then analyzed using a laboratory-designed function of IgorPro (both macro and function available upon request).

2.4. Electrophysiological recording

Patch-clamp recordings in the whole-cell mode were made using a patch-clamp amplifier with a capacitive headstage (Axoclamp 700B, Axon Instruments, Foster City, CA) using pipettes (3–5 M) of borosilicate glass (Sutter Instruments, Novato, CA) pulled using a P-97 Flaming–Brown pipette puller (Sutter Instruments, Novato, CA). Whole-cell recordings were low-pass-filtered at 3 kHz and digitized at 10 kHz. Data were digitized with a digitizer (ITC-18, Instrutech Inc., NY) and fed into a computer for off-line analysis (Apple Computer) using a laboratory arranged software on IgorPro (WaveMetrics Inc., OR, USA). Electrical stimulation were applied by constant current pulses (A395, WPI) through a glass microcapillary tube (5 μm inner diameter; filled with aCSF) placed in the stratum oriens (SO), stratum radiatum and stratum lacunosum-moleculare (SLM). Neurons were visualized by the oblique illumination with aid of contrast enhancement of a CMOS-camera (SKDCE-2EX, Sigma Koki Co., Tokyo, Japan) with an upright microscope (BX-51WI, Olympus Tokyo, Japan). In voltage-clamp mode, a test membrane potential step (-10 mV) were always applied prior to electrical stimulation, and traces with those series resistance (R_s) lower than $20\text{ M}\Omega$ were accepted.

The pipette solution consisted of, in mM: 130 Cs-MeSO₃, 10 Hepes, 4 MgCl₂, 4 NaATP, 0.4 NaGTP, 10 Na-Phosphocreatine, 10 EGTA; pH was adjusted to 7.2. 5 mM QX-314 was also added.

A glass microcapillary tube (5 μm inner diameter; filled with aCSF) was used as a recording electrode for field potential recordings.

The electrophysiological recording system was controlled by a procedure developed in Igor Pro (WaveMetrics Inc., OR, USA).

2.5. Neuron simulation

Numerical simulations were performed with NEURON (ver. 5.7) (Hines and Carnevale, 1997) on a Macintosh computer (Mac OSX). A realistic morphological and electrophysiological multi-compartment model of a CA1 pyramidal neuron was employed (Migliore et al., 1999; Migliore, 2003). The model consisted of 202 compartments representing the neuron's axon, soma, and dendrites. Please refer to the Neuron Model DB (<http://senselab.med.yale.edu/modeldb/ShowModel.asp?model=19696>) for the detail of the distribution and kinetics of the active conductance (g_{Na} , g_{KDR} , g_{KA} and g_{h}), and passive electrical properties of the components and synaptic connections embedded into the model. The simulated membrane potential response of each compartment was analyzed, and membrane potential profiles were drawn using IgorPro software and custom-made macros.

We calculated two different membrane potential profiles. In order to obtain two different membrane potential profiles for the case where the cell produces almost same amplitude of EPSP while one with action potential and the other without, we changed weight value in the model to seek the threshold. The resulted membrane potential profiles obtained just below the threshold (weight was 1.231×10^{-2} , see Fig. 4Ba) and above the threshold (weight was 1.24×10^{-2} , see Fig. 4Bb) showed almost similar amplitude and time course of EPSP (Fig. 4A).

The membrane potential profile of a population of cells (Fig. 4C) was calculated as an average of membrane potential ($V_{m_{\text{avg}}}$) as

function of distance from the soma (L) and proportion of the number of the non-excited cell relative to the excited cell (p) according to the equation below;

$$\frac{V_{m_{\text{avg}}}(L, p)}{p} = \frac{[(p-1)V_{m_{\text{epsp}}}(L) + V_{m_{\text{AP}}}(L)]}{p} \quad (1)$$

where $V_{m_{\text{epsp}}}(L)$ and $V_{m_{\text{AP}}}(L)$ are the membrane potential caused by the just below the threshold and just above the threshold, corresponding to the membrane potential profiles drawn in Fig. 4Ba and Bb respectively.

The PR ratio in Fig. 4D was calculated the ratio of the responses in SP ($L = 0 \mu\text{m}$) and those in SR ($L = 250 \mu\text{m}$), as a function of the proportion (p);

$$\text{PR ratio}(p) = \frac{V_{m_{\text{avg}}}(0, p)}{V_{m_{\text{avg}}}(250, p)} \quad (2)$$

The PR ratio for optical signal was calculated as the ratio of the amplitude of optical signal at $L = 0 \mu\text{m}$ and those at $L = 250 \mu\text{m}$.

3. Results

3.1. Amplitude distribution of neuronal responses in the optical signal

VSDs are molecular probes that convert membrane potential changes to changes in fluorescence. Fig. 1B–D shows a typical optical signal response when an electrical stimulus (250 μs , 200 μs in positive–negative direction) is applied to the Schaffer collaterals in area CA1 of the hippocampus (please see Tominaga et al., 2000, 2002).

Fig. 1B shows consecutive images of optical signals obtained at different times, starting from the stimulation. Representative traces of responses as a function of time, recorded at representative pixels are presented in the lower part of the panel. The left-most trace shows responses recorded at the stimulating site, showing that the stimulus artifact was followed by the postsynaptic response. The large arrow in this trace points to the peak of the stimulus artifact. Representative traces recorded from mid- and distal parts of CA1 are also indicated by large arrows. Because the peaks of individual optical traces appeared at different times due to propagation of the response, we used the peak amplitude as representative values in the following section to compare the amplitude of the response.

The time course of the optical signal along the somatodendritic axis of pyramidal cells is shown in Fig. 1C. The largest change appeared in the middle of SR, while in SP the peak was smaller and was followed by a hyperpolarizing response. The traces at each representative pixel are shown in Fig. 1D. Traces corresponding to different stimulus intensities are shown in pseudo-color code. Regardless of stimulus intensity, in SR responses were larger than those in other layers, whereas in SP responses were smaller, but hyperpolarizing responses were larger than those in other layers.

The distribution of the amplitude information was mapped (projected) onto a single frame in Fig. 1E, which shows the amplitude distribution of the maximum response (traces with arrows in Fig. 1B) at each pixel (maximum response map). Profiles of the maximum amplitude map along the somatodendritic axis of pyramidal cells are shown in Fig. 1F. The response profiles at different distances from the stimulating site (90, 180, 360, 540 μm) are shown. At each site, the peak response appeared in the middle of the SR (about 200 μm from the soma). The maximum response measured in stratum oriens was 70% or less of that measured in SR. This relationship was maintained across stimulus intensities (Fig. 1G and H); at each stimulus intensity, the peak amplitude of the optical signal was larger in SR.

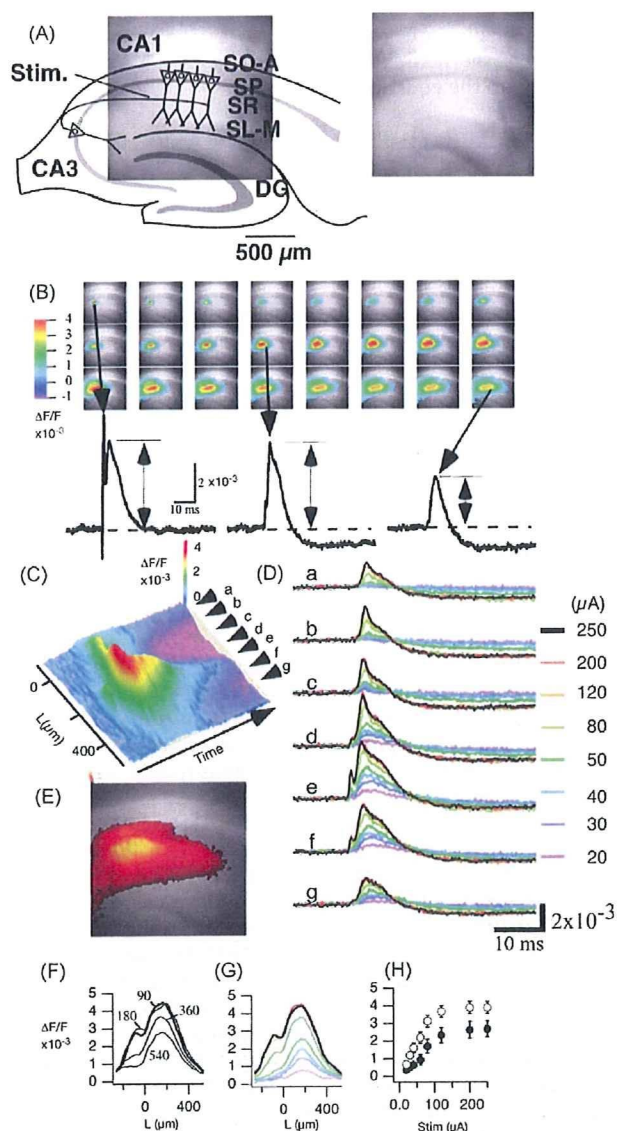


Fig. 1. Amplitude distribution of a Schaffer-collateral-evoked optical signal in area CA1 in the rat hippocampal slice preparation. (A) Schematic illustration of a rat hippocampal slice superimposed onto the fluorescent image of the recording area. The sampled area of the imaging system was about $1.8 \text{ mm} \times 1.8 \text{ mm}$. Stim., stimulation electrode; SO-A, stratum oriens-alveus; SP, stratum pyramidale; SR, stratum radiatum; SLM, stratum lacunosum-moleculare. (B) Consecutive images (left to right, top to bottom) showing optical signals obtained every 0.2 ms, starting from the stimulation. Lower traces are representative traces obtained at pixels in the indicated field of view. Arrows show the pixel where the signal showed a peak in the consecutive images. (C) A pseudo-colored three-dimensional graph of a slit recording of the optical signal in B obtained at about $90 \mu\text{m}$ from the stimulating electrode. (D) The representative traces of the optical signals recorded from representative pixels a–g in the slit image shown in panel C. The pseudo-colored traces in a–g represent responses to different stimulus intensities (20, 30, 40, 50, 80, 120, 200, 250 μA , respectively). (E) A pseudo-colored image of the projection of the maximum response at each pixel. (F) Maximum response profiles of the slice image in C (thick trace) and at slits at increasing distances (180, 360, 540 μm) from the stimulating electrode at different stimulus intensities. These color coded responses correspond to those shown in panel D. (G) Response profiles at $90 \mu\text{m}$ from the stimulating electrode at different stimulus intensities. These color coded responses correspond to those shown in panel D. (H) Stimulus–response relationships recorded from SR (open circles, $200 \mu\text{m}$ from the soma) and SP (filled circles) ($n = 6$ slices; bars, SEM). The data were acquired with a MiCAM ultima system sampling at a 10 kHz frame rate.

The soma responses should correspond to action potential firing in the pyramidal cell layer and should be over 100 mV of the membrane potential shift, while dendritic responses in SR should correspond to EPSPs and should be a few tens of millivolts of the membrane potential shift. If the response measured by VSD reflects the membrane potential amplitude, then we would expect larger responses in SP than in SR. In our optical recordings, however, we observed the opposite: Optical signals in SR were larger than those in SP. This observation raises the possibility that the VSD signal varies in sensitivity to membrane potential changes in different layers. If this were indeed the case, then it would be difficult to use VSD signals to compare the membrane potential response along the somatodendritic axis of pyramidal cells.

3.2. Changes in fluorescence caused by steady resting membrane depolarization show less VSD-signal-layer specificity

The apparent lack of correspondence between the amplitudes of the optical signal and actual membrane potential changes in SP and SR could be due to (1) tissue-dependent differences in VSD sensitivity, or (2) the population nature of the optical signal. To test these possibilities, we visualized steady fluorescence changes in response to experimental manipulation of $[\text{K}^+]_o$, which should cause tissue-independent, uniform depolarization of the resting membrane.

Switching the perfusate from control aCSF ($[\text{K}^+]_o = 2.5 \text{ mM}$) to a high- K^+ solution ($[\text{K}^+]_o = 25 \text{ mM}$) produced decreased fluorescence (Fig. 2A). Washing out the high- K^+ solution caused the responses to recover, with fluorescence levels returning to control levels. The distribution of the depolarizing response, as measured by a decrease in fluorescence, is shown in Fig. 2Ba. The ratio of the decrease relative to initial fluorescence (Fig. 2Ba) shows uniform changes in fluorescence in SR, while large changes occur in SP and SO (yellow-orange peaks orthogonal to the blue plane, Fig. 2B, panel a; also see Fig. 2C).

To test whether the large fluorescence change in SP and SO was caused by action potentials arising from postsynaptic cells, we added TTX to the high- K^+ perfusate (Fig. 2Bb). The steep peak disappeared when TTX was added to the high- K^+ solution (Fig. 2B, panel b). Profiles of the fluorescence changes along the somatodendritic axis of pyramidal cells are plotted in the graph of Fig. 2C and pooled data are plotted in the graph of Fig. 2D. These profiles show that the high- K^+ -associated (open circles) peak responses detected in SP and SO were greatly diminished by the application of TTX (filled circles). At each sampling point along the entire length of layers, the difference between pre-TTX and post-TTX was $p < 0.05$. This suggested that the peak was caused by action potential firing of neurons.

To exclude the effects of transmitter release from depolarized cells, we applied a cocktail containing major excitatory and inhibitory receptor blockers (50 μM APV, 10 μM CNQX, 20 μM bicuculline) to the high- K^+ perfusate (open triangles). The cocktail reduced the high- K^+ -depolarizing response ($p < 0.05$) in SR, SO, and stratum lacunosum-moleculare (SLM), suggesting that excess glutamate and/or GABA around the cells contributed in part to the depolarization we observed in slices bathed in high- K^+ solution. A peak near the soma region was abolished with TTX (filled triangles). Hence, this observation supports the possibility that the unequal distribution of fluorescence change in SP was caused mostly by action potentials from postsynaptic cells.

The steady and uniform fluorescence changes we observed in the absence of action potential (in TTX) imply that differences in layer-dependent VSD sensitivity may not be a major cause of the apparent mismatch between the optical signal amplitude and membrane potential response amplitude shown in Fig. 1.

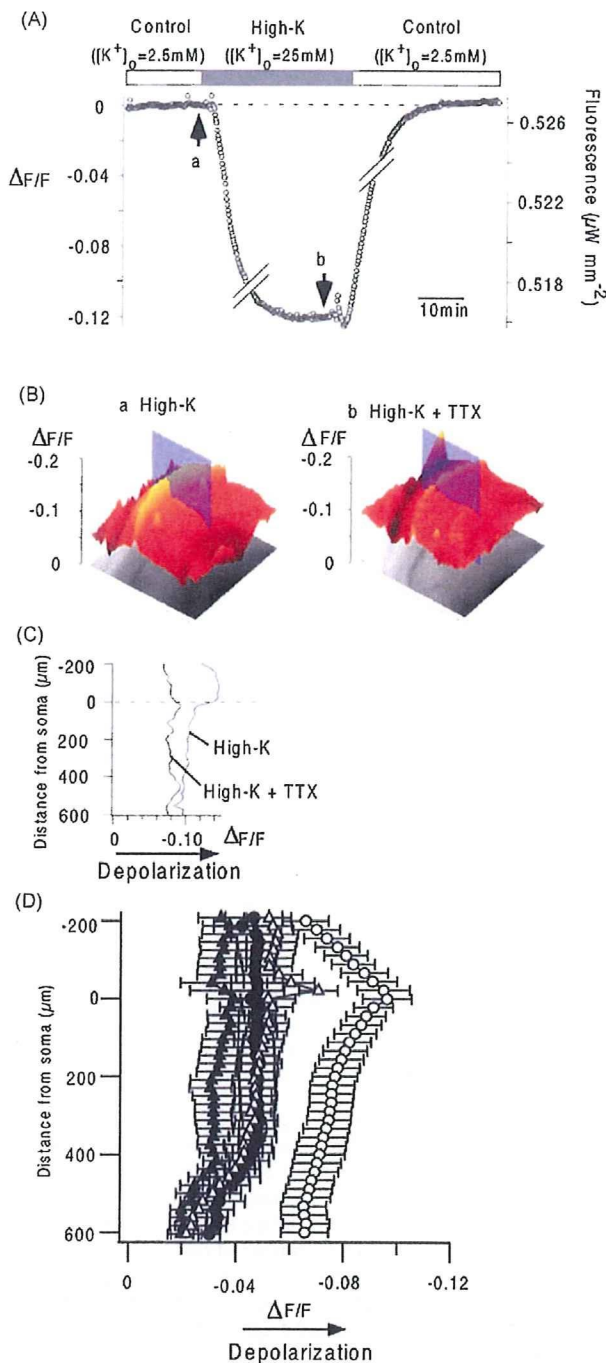


Fig. 2. Changes in VSD fluorescence measured in the middle of the SR of area CA1. (A) Relative fluorescence intensity ($\Delta F/F$) was measured and plotted against time. Each dot represents the average of 85 frames of fluorescent images obtained at a rate of 1 ms/frame and at 10 s intervals. The external solution was changed to a higher K^+ solution ($[K^+]_o = 25$ mM) from normal aCSF ($[K^+]_o = 2.5$ mM) for 30 min. The absolute fluorescence intensity is indicated in the right axis. Arrows labeled a and b point to the representative frames used for constructing the graphs in panel B. (B) The effect of TTX on the distribution of fluorescence changes in response to stimulation with high- K^+ solution. Three-dimensional graphs showing the amplitude of responses to high- K^+ solution in the absence (a) and presence (b) of TTX. TTX decreased the amplitude of responses, as reflected by a decrease in fluorescence. (C) Profiles of fluorescence changes along the somatodendritic axis of pyramidal cells in the absence (high- K^+) and presence of TTX (high- K^+ + TTX). (D) Pooled data of fluorescence changes under high- K^+ (open circles) and high- K^+ + TTX (filled circles) conditions. The other set of data show the changes after application of APV, CNQX, and bicuculline without TTX (open triangles) and with TTX (filled triangles). Data are means \pm SEMs ($n = 4$ –9 slices).

3.3. The distribution of membrane potential responses along the somatodendritic axis of pyramidal cells as simulated with the NEURON simulator was similar to the membrane potential profiles measured in slices bathed in high- K^+ solution

The population nature of the optical signal may underlie the apparent mismatch between the optical signal amplitude and membrane potential response amplitude. To test whether this is the case, we changed the composition of a population of cells so that it comprised cells that fire action potentials and those that do not when stimulated by a single electrical shock to the Schaffer collaterals. Since it is difficult to identify these cells and alter the population of cells accordingly, we used a realistic numerical model of a hippocampal CA1 pyramidal neuron (Migliore et al., 1999) to simulate the distribution of membrane potential responses in area CA1. The software we used is called NEURON (Hines and Carnevale, 1997). Fig. 3A illustrates this model in terms of a tree-like drawing showing the topographical geometry of the CA1 pyramidal neuron we modeled. The traces in Fig. 3A show representative membrane potential responses at different sites (0, 100, 200, and 300 μ m from the soma) in response to a relatively strong synaptic input. The membrane potential responses in different segments were used to estimate the distribution of the response along the somatodendritic axis of the cell using information about the digital morphological reconstructions of the cell.

Fig. 3B shows the membrane potential response profiles along the somatodendritic axis of the CA1 pyramidal neuron we calculated using the simulation results when either a just-above threshold or a just-below threshold input was provided. In this model, the synapses terminated 200 μ m from the soma. Thus, we could reproduce the membrane potential profiles of cells that fire action potentials (Fig. 3Ba) and of those that do not fire action potentials (Fig. 3Bb) but have almost identical EPSP amplitudes.

The membrane potential responses along the somatodendritic axis of the pyramidal cell are shown in the three-dimensional (3D) graphs of Fig. 3B. Although the size of the EPSP was almost identical, the overall potential profiles were quite different. When the pyramidal cell fired an action potential, very strong responses (almost 80 mV) occurred in SP and SO, and rather small (40 mV) responses occurred in the middle part of the apical dendrite ($L = 300$ μ m) (Fig. 3Ba). On the other hand, when the pyramidal cell did not fire an action potential, small responses occurred in the middle part of the dendrite (Fig. 3Bb). Both of these simulations did not resemble the amplitude and distribution of responses we obtained by optical recording (cf. Fig. 1).

3.4. Reducing the proportion of excited neurons can mimic the profile of responses obtained by the optical recording method

Fig. 4 shows membrane potential response profiles calculated from our simulated results. We simulated membrane potential responses to apical dendritic synaptic input that was just below threshold for action potential generation (EPSP only; gray trace in Fig. 4A) and to synaptic input that was just above threshold (EPSP followed by an action potential; black trace in Fig. 4A). The distribution of peak membrane potential changes along the somatodendritic axis of the modeled pyramidal neuron is shown in Fig. 4B (panels a and b, respectively). It is clear from the figure that the shapes of the two membrane potential profiles are quite different. When the pyramidal cell received just-above threshold input that elicited an action potential, the membrane potential responses over SP (distance < 0 μ m from the soma) showed a large plateau; the tail-end of the response at the apical dendrite showed no obvious peak (Fig. 4B, panel b). On the other hand, when the pyramidal cell received just-below threshold input that failed to

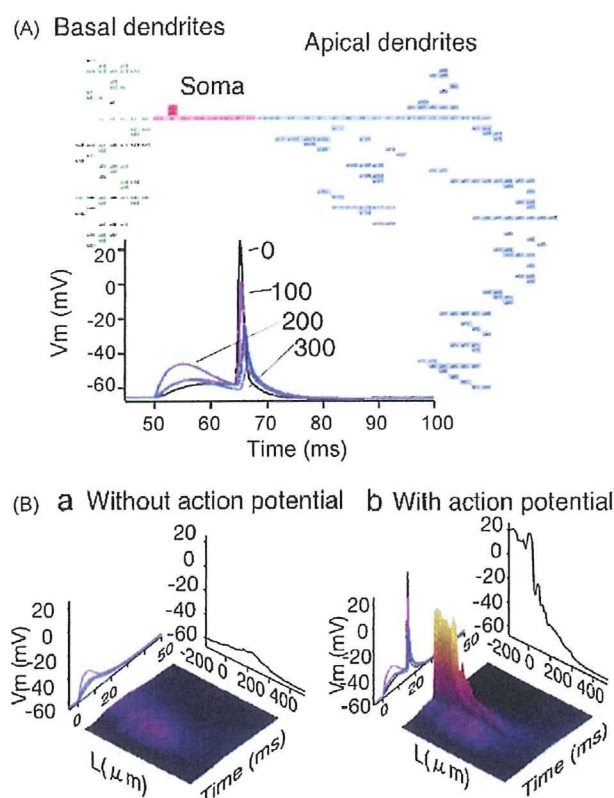


Fig. 3. (A) A realistic multi-compartment model of a pyramidal cell. Each segment has its own electrophysiological characteristics. The graph shows membrane potential responses of different segments located at different distances from the soma. The membrane potential responses were calculated from our model using the NEURON simulator program (Hines and Carnevale, 1997). (B) Time course of representative profiles of membrane potential changes along the somatodendritic axis of a CA1 pyramidal neuron in response to a weak synaptic input that fails to cause an action potential at the soma (a) and to a strong synaptic input that causes an action potential at the soma (b). These profiles were calculated by averaging the membrane potential responses measured from each compartment of the neuron model. Each 3D graph contains linear plots showing the kinetics of membrane potential changes (left) and the peak membrane potential profiles (right).

elicit an action potential, the membrane responses at the middle of SR (distance = 250 μm) showed a small peak (Fig. 4B, panel a). The model employed here is a realistic model neuron that had “active” apical dendrites (Magee and Johnston, 1995; Migliore et al., 1999; Johnston et al., 2003). For the input condition that produced an action potential, the ratio of the membrane potential amplitude in SP to that in SR was 5.13, whereas for the input condition that failed to produce an action potential, this ratio was 0.63. That is, the response was five times larger in SP than in SR when the cell generated only an EPSP (Fig. 4Ba), the response in SP was smaller than that in SR.

Fig. 4C shows the profiles of averaged responses when the number of the cells was changed to contain fewer excited neurons (i.e., neurons that generated action potentials; Fig. 4Bb) relative to non-excited neurons (i.e., neurons that generated only EPSPs; Fig. 4Ba) (see Section 2). The shape of the membrane potential profile in Fig. 4C resembled the shape of the membrane potential profile reflected in the optical signal (Figs. 1F,G and 5B). On the other hand, changing the timing of the action potential firing within the range of 16 ms randomly did not affect the shape of the profile much (Fig. 4C blue). Fig. 4D shows the PR ratio, the ratio of the responses in SP ($L = 0 \mu\text{m}$) and those in SR ($L = 250 \mu\text{m}$), as a function of different excited cell-to-non-excited cell proportions (p ; see Section 2). The PR ratio

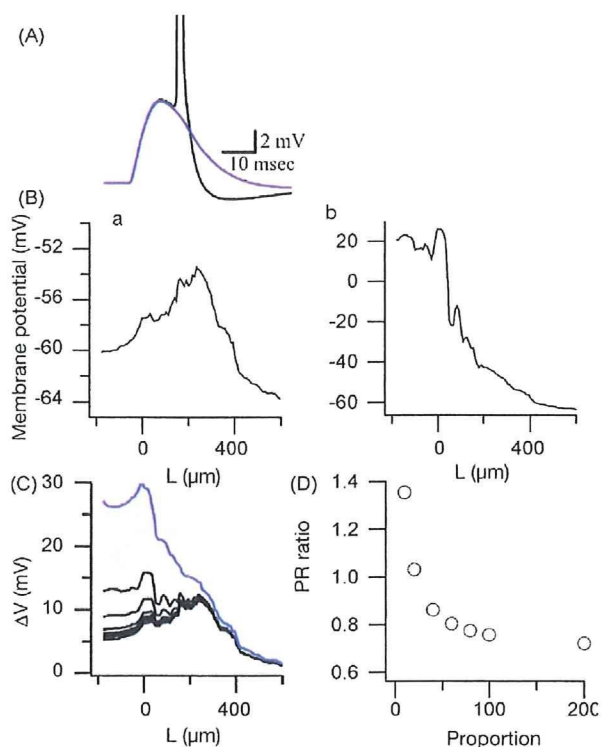


Fig. 4. Profiles of membrane potential responses to simulated synaptic input. (A) Traces representing membrane potential changes at the soma, as simulated using NEURON. The black trace represents responses to a just-above threshold synaptic input; the blue trace represents responses to a just-below threshold input. (B) Membrane potential profiles along the somatodendritic axis of the modeled pyramidal cell when it received just-below threshold input (a) and just-above threshold input (b). (C) Black traces show average membrane potential profiles of a modeled pyramidal cell when the network comprised different proportions of excited and non-excited cells (1:10, 1:20, 1:40, 1:60, 1:80, 1:100, 1:200), i.e., a neuron that fired an action potential (Ba) or one that did not fire an action potential (Bb). A blue trace shows membrane potential profile when the action potential firing show random jitter within a range of 16 ms. (D) Changes in the PR ratio, the ratio of membrane potential responses in SP (soma; $L = 0 \mu\text{m}$) relative to those in SR (dendrites; $L = 250 \mu\text{m}$), caused by changing the proportion of excited cells and non-excited cells. See Section 2 for detail.

decreased as we reduced the proportion of excited cells to non-excited cells. When the model comprised one excited cell among 10 cells, the PR ratio was 1.35. However, when the model comprised one excited cell among 200 cells, the PR ratio decreased to 0.72. We chose the latter model to contain 200 cells because this is the maximum number of cells viewable with our imaging system, which covers an area of about $25 \mu\text{m} \times 25 \mu\text{m}$ at the objective plane. The number of cells, therefore, covered by a single pixel should not exceed 200 cells, assuming that the diameter of a cell is $10 \mu\text{m}$ and the optical signal covers a depth of $200 \mu\text{m}$ (de Curtis et al., 1999).

For the optical signal shown in Fig. 1E, the PR ratio was about 0.73, which was higher than PR ratios calculated in our simulations and higher than PR ratios calculated from pooled optical recording data (0.67 ± 0.07 , mean \pm SEM; $n = 6$ slices; Fig. 5C, open circles). The PR ratio was calculated as a ratio of the ratio of the amplitude of optical signal at soma layer ($L = 0 \mu\text{m}$) and those at middle of SR ($L = 250 \mu\text{m}$). Fig. 5C (open circles) shows the PR ratios from pooled data as a function of stimulus intensity. The PR ratio first decreased as stimulus intensity increased, then increased, reaching a maximum of 0.7. The decrement of the PR ratio at lower stimulus intensities suggests that the membrane potential profile might reflect feed-forward inhibition activated by Schaffer collateral stimulation (Alger and Nicoll, 1982b; Turner, 1990).

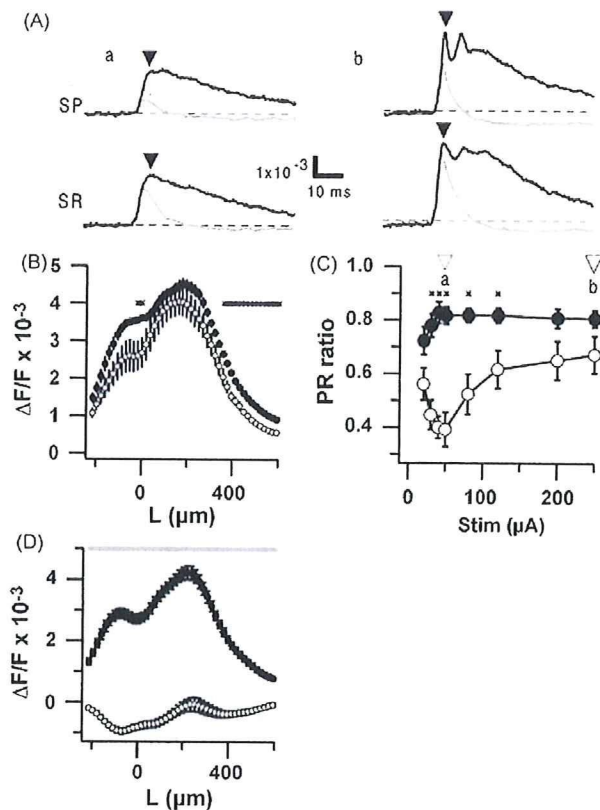


Fig. 5. (A) Time course of optical signals recorded from slices bathed in normal aCSF and after application of PITX. Responses to a weak stimulus ($50 \mu\text{A}$) (a) and responses to a strong stimulus ($250 \mu\text{A}$) (b) are shown. Black traces show the time course in the presence of PITX; gray traces represent controls. SP, traces obtained at a pixel corresponding to SP; SR, traces obtained at a pixel in the middle of SR. (B) Membrane potential profiles obtained from pooled optical recording data. The membrane potential responses were recorded $90 \mu\text{m}$ from the stimulating site. Open circles, slices bathed with normal aCSF (control); filled circles, slices treated with $100 \mu\text{M}$ PITX. (C) Changes in the PR ratio of optical signal as a function of stimulus intensity ($n = 6$ slices; error bars, SEM). Open circles, slices bathed with normal aCSF (control); filled circles, slices treated with $100 \mu\text{M}$ PITX. Open arrowheads (a and b) show the stimulus intensities corresponding to traces in panel A. (D) Membrane potential profile $25\text{--}30$ ms following stimulation of control (open circles) and $100 \mu\text{M}$ PITX-treated (filled circles) slices. Asterisks on traces (B, C, D) indicate significant differences between profiles recorded under control and PITX treatment conditions (ANOVA, $P < 0.05$).

3.5. Optical signals revealed the impact of feed-forward inhibition on signal propagation in the area CA1 circuit in response to SR stimulation

The firing of principal neurons in area CA1 are thought to be under the control of feed-forward inhibitory inputs in addition to feedback types of control in the circuit (Buzsáki, 1984). In feed-forward inhibition the amount of inhibition is not controlled by the activation of postsynaptic principal neurons. To determine how inhibitory inputs affect membrane potential changes along the somatodendritic axis of a pyramidal cell upon SR stimulation, we applied PITX, a GABA_A receptor inhibitor, to the aCSF solution bathing the hippocampal slices and monitored optical signals in SP and SR of area CA1 (Fig. 5).

The effect of PITX on the optical signal is shown in Fig. 5A. PITX increased the amplitude of the optical signals and prolonged the response. We defined the increase in the first peak of the response (filled arrowheads in Fig. 5A) caused by PITX application as feed-forward inhibition, because this increase preceded the action potential firing of the postsynaptic cells (see also Fig. 1D). The effect of feed-forward inhibitory inputs along the somatodendritic

axis is also shown in Fig. 5B as membrane potential profiles of the first peak, in which the application of PITX increased responses significantly in the perisomatic region ($-20 \mu\text{m} < L < 0 \mu\text{m}$) and distal apical dendritic region ($L > 360.1 \mu\text{m}$) (ANOVA, $p < 0.05$). Responses in SR, however, remained almost the same as in the control condition.

To show control over action potential firing, we plotted PR ratios (Fig. 5C). The initial decrease in PR ratio was abolished by adding $100 \mu\text{M}$ PITX to the aCSF (Fig. 5C, filled circles). That is, as the EPSP increased, spike activation probability increased in the presence of PITX. For comparison with feed-forward inhibition phase, changes in the falling phase (30 ms after stimulation) of the response are shown in Fig. 5D. A hyperpolarizing response was seen in SO and on apical dendrites $400 \mu\text{m}$ from somatic and perisomatic regions. As is clear in the figure, the hyperpolarizing response was replaced with a depolarizing response that occurred along the entire length of the somatodendritic axis. This could mostly reflect the impact of feedback inhibition on pyramidal cell activity.

3.6. Optical signals revealed the impact of feed-forward inhibition on signal propagation in the area CA1 circuit in response to SLM and SO stimulation

To examine the amount feed-forward inhibitory control contributed by major input pathways, we assessed membrane potential profiles in response to SLM and SO stimulation (Fig. 6).

PITX application significantly enhanced the SLM stimulation-induced response in both perisomatic and distal apical dendritic regions, as was seen with SR stimulation (Fig. 6B). Significant differences (asterisks; $P < 0.05$) were also observed in SO and in perisomatic ($-200 \mu\text{m} < L < 126.2 \mu\text{m}$) and distal apical dendritic regions ($L > 381.3 \mu\text{m}$). It is interesting to note that changes in the PR ratio after SLM stimulation (Fig. 6C) were quite different from changes in the PR ratio after SR stimulation (Fig. 5C), even though both reflect perisomatic inhibition (cf. Figs. 5B and 6B). Upon SLM stimulation, inhibition in the perisomatic region increased as stimulus intensity increased, as shown in Fig. 6C, and was significantly different ($P < 0.05$) at stimulus intensities greater than $120 \mu\text{A}$. SO stimulation induced larger responses in SO and in somatic regions. Although PITX application failed to appreciably affect these responses, PITX affected responses recorded in distal dendrites, with significant differences observed in regions farther than $258.8 \mu\text{m}$ from the soma. This can also be seen in the PR ratio shown in Fig. 6G. After-hyperpolarization in the perisomatic region was clear and PITX treatment induced full-range depolarization along the somatodendritic axis.

3.7. Electrophysiological recording and stimulation

Fig. 7 shows the representative current responses of a pyramidal cell in the area CA1 upon the SR, SLM and SO stimulation at two different stimulus intensities ($250 \mu\text{A}$ and $40 \mu\text{A}$) at different holding potentials (-90 mV to -20 mV). Stimulation elicited a mixture of excitatory postsynaptic current (EPSC) and inhibitory postsynaptic current (IPSC). As is clear in the Fig. 7A SR stimulation most right-hand expanded traces at depolarized holding potential (-30 mV), a weak stimulation ($40 \mu\text{A}$) caused only fast feed-forward IPSC following a sharp small inward EPSC, while increasing stimulation intensity to $250 \mu\text{A}$ additionally recruited following feedback IPSC (Glickfeld and Scanziani, 2006). This was not clear in SO stimulation and SLM stimulation (Fig. 7B SO and C SLM). The IPSC was not clearly seen on the traces at -70 mV, since the calculated reversal potential for chloride ion (E_{Cl}) was about -73 mV. All the cells tested ($n = 6$) showed similar tendency.

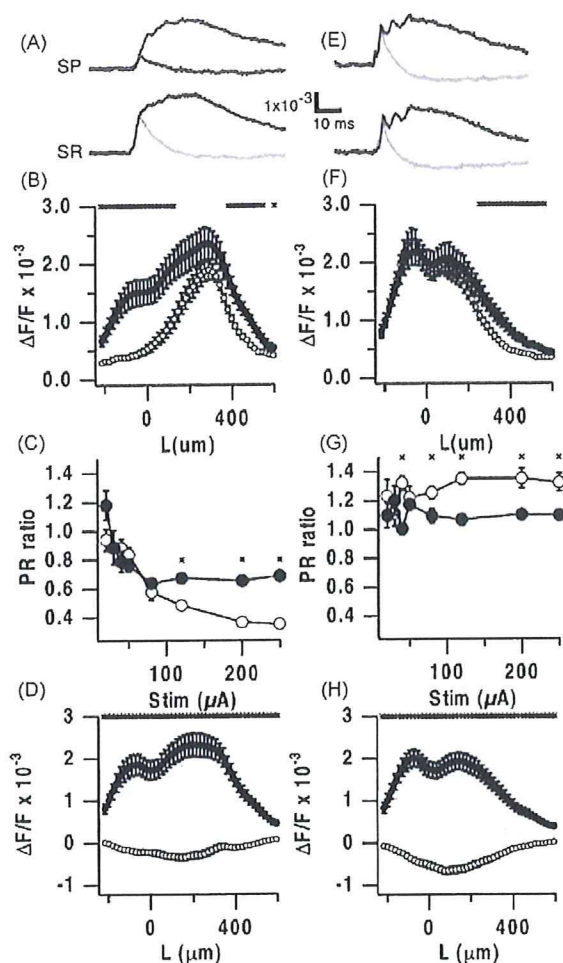


Fig. 6. (A, E) Time course of optical signals recorded from slices bathed in normal aCSF and after application of PITX following SLM stimulation (A) and SO stimulation (E). Black traces show the time course in the presence of PITX; gray traces represent controls. SP, traces obtained at a pixel corresponding to SP; SR, traces obtained at a pixel in the middle of SR. (B, F) Membrane potential profiles obtained from pooled optical recording data for SLM stimulation (B) and SO stimulation (F). The membrane potential responses were recorded 90 μm from the stimulating site. Open circles, slices bathed with normal aCSF (control); filled circles, slices treated with 100 μM PITX. (C, G) Changes in the PR ratio after SLM stimulation (C) and after SO stimulation (G) as a function of stimulus intensity ($n = 7$ slices; error bars, SEM). Open circles, slices bathed with normal aCSF (control); filled circles, slices treated with 100 μM PITX. (D, H) Membrane potential profiles 25–30 ms of control (open circles) and in 100 μM PITX-treated (filled circles) slices following SLM stimulation (D) and SO stimulation (H). These profiles were obtained from pooled optical recording data. Asterisks on traces (B, C, D, F, G, H) indicate significant differences between profiles recorded under control and PITX treatment conditions (ANOVA, $P < 0.05$).

4. Discussion

In the present study, we have shown that optical recording with VSD can be used to measure membrane potential responses of pyramidal cells in area CA1 of the hippocampal slice after stimulating the Schaffer collateral pathway. This method allowed us to demonstrate the impact of a feed-forward inhibitory circuit on signal propagation following Schaffer collateral activation (Fig. 5). It is rather difficult to show the amount of neuronal activity affected by feed-forward inhibitory pathways because available methods are limited in their ability to detect neuronal activity sensitive to inhibitory actions (Turner, 1990).

The reduction of PR ratios (Fig. 5C) at lower stimulus intensities and the blockade of this reduction by PITX

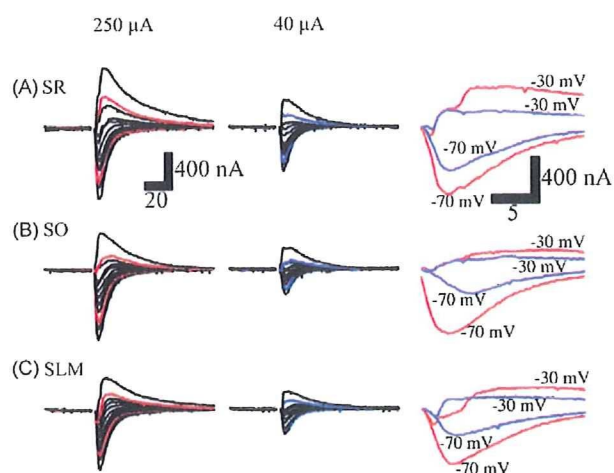


Fig. 7. Voltage-clamp recording from a pyramidal cell in response to SR stimulation (A), SO stimulation (B) and SLM stimulation (C) at two different stimulus intensities (250 μA ; left column) and (40 μA ; center column) at different holding potentials at -80 , -75 , -70 , -65 , -60 , -55 , -50 , -45 , -40 , -35 , -30 and -20 mV. The expanded and superimposed traces at right-most column show the current response at depolarized condition (-30 mV) and near the resting membrane potential (-70 mV) upon strong stimulus (250 μA ; red) and weak stimulus (40 μA ; blue). Stimulation was applied about 90 μm from the pyramidal cell under whole-cell clamp condition.

corresponds with observations that weak orthodromic stimuli can evoke IPSPs (Andersen et al., 1969a; Turner, 1988, 1990) and IPSC (see Fig. 7A). PITX-induced changes in the membrane potential profiles were mainly observed in SP, not SR (Fig. 5B). This might be caused by a change in the probability of action potential firing, as predicted by our simulation model (Fig. 4C). Much electrophysiological and anatomical evidence exists that shows feed-forward inhibition affects pyramidal cell excitability through inhibitory synaptic terminals in SP (Alger and Nicoll, 1982b; Buzsáki, 1984; Lacaille and Schwartzkroin, 1988a,b; Turner, 1990; Cobb et al., 1997; Megias et al., 2001). Feed-forward inhibition is thought to make possible the precise control of spike firing timing (Pouille and Scanziani, 2001, 2004). Our findings show that optical recording methods can allow us to visualize the degree of inhibition in an intact neuronal circuit, which is often difficult to access through traditional electrophysiological methods (Verheugen et al., 1999).

The inhibitory network in the hippocampus consists of many kinds of interneurons (Buhl et al., 1994; Freund and Buzsáki, 1996) and plays a crucial role in brain function, especially in memory formation and retrieval, by causing oscillations (Buzsáki, 2002; Mann and Paulsen, 2005, 2006). Oscillations depend on the time-dependent phasic regulation of unequally distributed excitatory and inhibitory inputs along the somatodendritic axis of a pyramidal cell (Megias et al., 2001) and act as “dipoles” (Buzsáki, 2002). The ability to measure somatodendritic membrane potential profiles with VSD-optical recording methods will be useful to reveal the dynamics of inhibitory networks (Mann et al., 2005b).

The SLM stimulation (Figs. 6B and 7B) elicited smaller optical response compared to that to SR stimulation (Fig. 5B). This may reflect the smaller temporoammonic pathway (TA pathway) fEPSP response to SLM stimulation (Remondes and Schuman, 2002, 2003), although our SLM stimulation may contain contamination of Schaffer collateral stimulation. Please note that the response caused by SO stimulation shown in Figs. 6E–H and 7C did not include fraction of the response caused by direct stimulation of pyramidal cells, since the response was not seen under the blockade of glutamergic synaptic connection. They are mostly

reflecting the back propagation of action potential firing of the pyramidal cells caused by synaptic transmission to the basal dendrite when the stimulus intensity was strong.

The stimulus–response relationships, as reflected in the PR ratios, following SR and SLM stimulation (Figs. 5C and 6C) were quite different. That is, the PITX effect reached maximum levels at lower stimulus intensities during SR stimulation (Fig. 5C), while the effect reached maximum levels at higher stimulus intensities during SLM stimulation (Fig. 6C). Since both modes of stimulation induced significant inhibition in the perisomatic region while sparing responses from the center of the apical dendrite, the differences in PR ratios may be due to differential control of feed-forward inhibition to the perisomatic region. The input pathways to CA1 vary such that SR receives inputs from CA3 whereas SLM receives inputs from entorhinal cortex. Thus, the differences we observed may be due to differences in synaptic action on the same class of interneurons (Kajiwara et al., 2008) or may reflect the recruitment of different classes of inhibitory interneurons. This difference may be due to differential control of CA1 pyramidal cell excitation, since SR receives inputs from CA3 whereas SLM receives inputs from entorhinal cortex. On the other hand, feed-forward inhibition was not observed in perisomatic regions after SO stimulation, even though it was detected in distal dendritic regions. This difference may be due to the fact that SO contains inputs from recurrent collaterals and to a lesser extent from Schaffer collaterals. The role of these different types of feed-forward inhibition in the CA1 network should be examined further in detail.

4.1. Does $\Delta F/F$ reflect the amount of membrane potential change in different membrane compartments?

Evaluating the size of optical signals has continued to be problematic, ever since VSD (WW-401) was first used for optical recording in mammalian brain slice preparations (Grinvald et al., 1982). Moreover, it was uncertain whether optical signal amplitude varied in different tissue components. $\Delta F/F$ is usually used to calibrate optical signals to some extent according to fluorescent dye (e.g., RH-796, RH-418, Di-4-ANEPPS, Di-8-ANEPPS). These measures are based on the observations that optical signals change proportionally according to membrane potential changes (Conti and Tasaki, 1970; Cohen et al., 1974; Ross et al., 1977) and that the proportionality constant of a single membrane or a single cell is the same. Evaluating the amplitude of an optical signal in tissues is more difficult because we cannot simply assume that fluorescence intensity actually reflects dye in the membranes in which we want to measure membrane potentials. We can classify a dye that has incorporated into neuronal tissue into three categories depending on where the dye is incorporated: (1) dyes that incorporate into neuronal membranes (active neuronal dye); (2) dyes that incorporate into glial membranes (active glial dye); and (3) dyes that incorporate into dead cells, connective tissues, and other lipids (inactive dye). The latter class of dyes should not show membrane potential changes. If we want to visualize fast neuronal responses via VSD signals, the second and third classes of dye should appear as offsets (F_{offset}). These offsets increase only the denominator of an optical signal, and thus decrease the dye's sensitivity to membrane potential changes, i.e., $\Delta F/F$ becomes smaller. In other words, even if the same membrane potential change occurs in neurons in a tissue, $\Delta F/F$ can vary depending on the characteristics of the tissue if F_{offset} is different.

When hippocampal slices were stimulated with a high- K^+ solution and treated with TTX, the changes in fluorescence were almost equal in different layers (Fig. 2D). This suggests that, at least in area CA1, the specificity of the dye for different layers (SO, SP, SR, SLM) is fairly similar. This implies that the second and third class of dyes behave similarly in different layers.

We do not know how the second class of dyes (glial dyes) affects optical signals, but it seems that how a dye affects optical signals largely depends on the dye itself. Non-fluorescent dyes, which are visualized through absorption changes at certain wavelengths (e.g., RH-155), have been reported to be more sensitive to glial membrane potential changes (Kojima et al., 1999; Kawamura et al., 2004). Unlike Kojima and colleagues, however, we observed almost no effect on optical signal time course in response to a glial transporter inhibitor (Tominaga et al., 2002). In addition, their optical signals often lacked hyperpolarizing signals that follow the EPSP–action potential response. On the other hand, using optical recording, we observed GABA_A receptor antagonist-sensitive IPSPs that are observable in intracellular recordings (Figs. 1D and 5D and also see Fig. 5 in Tominaga et al., 2000). Thus, signals observed with RH-155 would not be detected by Di-4-ANEPPS, the fluorescent dye we used in the present study (Chang and Jackson, 2003).

4.2. The population nature of the optical signal

Our simulation results (Fig. 4) show that the optical signal may be influenced by the neuronal makeup of the network. In our neural network model of area CA1, we changed only the proportion of cells firing action potentials (excited cells) to those not producing action potentials (non-excited cells). The ratio of excited to non-excited cells needed to be reduced to 1:100 so that the membrane potential profile was similar to the optical signal. This big difference in the number of excited cells versus non-excited cells should decrease if we incorporate into the model randomness in the timing of action potentials. This should be examined in future experiments. In order to minimize introduction of assumptions on the population activity, we had to use extremely simplified binary population calculated with single NEURON model. This, in turn, could exclude some aspects of dendritic membrane potential dynamics (Golding and Spruston, 1998; Sjostrom et al., 2008). Although our simulation showed that the population nature could, at least in part, explain the distribution of optical signal, further details of the actual spatio-temporal dynamics of the membrane potential response should be examined elsewhere.

Our simulations indicate that the population nature of the optical signal may be useful in detecting the synchronicity of action potentials in a neuronal circuit, which is often important for representing information in the brain (Mann et al., 2005b; Schaefer et al., 2006). It would also be useful to visualize how inhibitory inputs actually act within the neuronal circuit during memory formation and retrieval (Buzsáki, 2002). Once optical signals are confirmed to be accurate representations of population signals, then because of its simplicity, optical recording should be promoted as a useful method for evaluating neuronal information processing based on a balance of excitatory and inhibitory inputs to neurons (Liu, 2004).

GABAergic transmission in the CNS has great importance in terms of the development of pharmacological targets for treating various mental disorders. A robust recording method like optical recording to monitor the inhibitory activity of neuronal tissue should provide one solution to the growing demands for quick and comprehensive assay methods for physiological responses.

References

- Aihara, T., Kobayashi, Y., Tsukada, M., 2005. Spatiotemporal visualization of long-term potentiation and depression in the hippocampal CA1 area. *Hippocampus* 15, 68–78.
- Alger, B.E., Nicoll, R.A., 1982a. Pharmacological evidence for two kinds of GABA receptor on rat hippocampal pyramidal cells studied in vitro. *J. Physiol. (Lond.)* 328, 125–141.
- Alger, B.E., Nicoll, R.A., 1982b. Feed-forward dendritic inhibition in rat hippocampal pyramidal cells studied in vitro. *J. Physiol. (Lond.)* 328, 105–123.

- Andersen, P., Eccles, J.C., Loynning, Y., 1963. Recurrent inhibition in the hippocampus with identification of the inhibitory cell and its synapses. *Nature* 198, 540–542.
- Andersen, P., Eccles, J.C., Loynning, Y., 1964. Pathway of postsynaptic inhibition in the hippocampus. *J. Neurophysiol.* 27, 608–619.
- Andersen, P., Gross, G.N., Lomo, T., Sveen, O., 1969a. Participation of inhibitory and excitatory interneurons in the control of hippocampal cortical output. *UCLA Forum Med. Sci.* 11, 415–465.
- Andersen, P., Bliss, T.V., Lomo, T., Olsen, L.I., Skrede, K.K., 1969b. Lamellar organization of hippocampal excitatory pathways. *Acta Physiol. Scand.* 76, 4A–5A.
- Andersen, P., Dingledine, R., Gjerstad, L., Langmoen, I.A., Laursen, A.M., 1980. Two different responses of hippocampal pyramidal cells to application of gamma-aminobutyric acid. *J. Physiol. (Lond.)* 305, 279–296.
- Antic, S., Zecevic, D., 1995. Optical signals from neurons with internally applied voltage-sensitive dyes. *J. Neurosci.* 15, 1392–1405.
- Antic, S.D., 2003. Action potentials in basal and oblique dendrites of rat neocortical pyramidal neurons. *J. Physiol.* 550, 35–50.
- Barish, M.E., Ichikawa, M., Tominaga, T., Matsumoto, G., Iijima, T., 1996. Enhanced fast synaptic transmission and a delayed depolarization induced by transient potassium current blockade in rat hippocampal slice as studied by optical recording. *J. Neurosci.* 16, 5672–5687.
- Brown, T.H., Johnston, D., 1983. Voltage-clamp analysis of mossy fiber synaptic input to hippocampal neurons. *J. Neurophysiol.* 50, 487–507.
- Buhl, E.H., Han, Z.S., Lorinczi, Z., Stezhka, V.V., Kamup, S.V., Somogyi, P., 1994. Physiological properties of anatomically identified axo-axonic cells in the rat hippocampus. *J. Neurophysiol.* 71, 1289–1307.
- Buzsáki, G., 1984. Feed-forward inhibition in the hippocampal formation. *Prog. Neurobiol.* 22, 131–153.
- Buzsáki, G., 2002. Theta oscillations in the hippocampus. *Neuron* 33, 325–340.
- Chang, P.Y., Jackson, M.B., 2003. Interpretation and optimization of absorbance and fluorescence signals from voltage-sensitive dyes. *J. Membr. Biol.* 196, 105–116.
- Chang, P.Y., Jackson, M.B., 2006. Heterogeneous spatial patterns of long-term potentiation in rat hippocampal slices. *J. Physiol.* 576, 427–443.
- Cobb, S.R., Halasy, K., Vida, I., Nyiri, G., Tamas, G., Buhl, E.H., Somogyi, P., 1997. Synaptic effects of identified interneurons innervating both interneurons and pyramidal cells in the rat hippocampus. *Neuroscience* 79, 629–648.
- Cohen, L.B., Salzberg, B.M., Davila, H.V., Ross, W.N., Landowne, D., Waggoner, A.S., Wang, C.H., 1974. Changes in axon fluorescence during activity: molecular probes of membrane potential. *J. Membr. Biol.* 19, 1–36.
- Conti, F., Tasaki, I., 1970. Changes in extrinsic fluorescence in squid axons during voltage-clamp. *Science* 169, 1322–1324.
- Davie, J.T., Kole, M.H., Letzkus, J.J., Rancz, E.A., Spruston, N., Stuart, G.J., Hausser, M., 2006. Dendritic patch-clamp recording. *Nat. Protoc.* 1, 1235–1247.
- de Curtis, M., Takashima, I., Iijima, T., 1999. Optical recording of cortical activity after in vitro perfusion of cerebral arteries with a voltage-sensitive dye. *Brain Res.* 837, 314–319.
- Dingledine, R., Langmoen, I.A., 1980. Conductance changes and inhibitory actions of hippocampal recurrent IPSPs. *Brain Res.* 185, 277–287.
- Dingledine, R., Gjerstad, L., 1980. Reduced inhibition during epileptiform activity in the in vitro hippocampal slice. *J. Physiol.* 305, 297–313.
- Freund, T.F., Buzsáki, G., 1996. Interneurons of the hippocampus. *Hippocampus* 6, 347–470.
- Glickfeld, L.L., Scanziani, M., 2006. Distinct timing in the activity of cannabinoid-sensitive and cannabinoid-insensitive basket cells. *Nat. Neurosci.* 9, 807–815.
- Golding, N.L., Spruston, N., 1998. Dendritic sodium spikes are variable triggers of axonal action potentials in hippocampal CA1 pyramidal neurons. *Neuron* 21, 1189–1200.
- Griffith, W.H., Brown, T.H., Johnston, D., 1986. Voltage-clamp analysis of synaptic inhibition during long-term potentiation in hippocampus. *J. Neurophysiol.* 55, 767–775.
- Grinvald, A., Manker, A., Segal, M., 1982. Visualization of the spread of electrical activity in rat hippocampal slices by voltage-sensitive optical probes. *J. Physiol.* 333, 269–291.
- Hines, M.L., Carnevale, N.T., 1997. The NEURON simulation environment. *Neural Comput.* 9, 1179–1209.
- Inoue, M., Hashimoto, Y., Kudo, Y., Miyakawa, H., 2001. Dendritic attenuation of synaptic potentials in the CA1 region of rat hippocampal slices detected with an optical method. *Eur. J. Neurosci.* 13, 1711–1721.
- Johnston, D., Christie, B.R., Frick, A., Gray, R., Hoffman, D.A., Schexnayder, L.K., Watanabe, S., Yuan, L.L., 2003. Active dendrites, potassium channels and synaptic plasticity. *Philos. Trans. R. Soc. Lond. B Biol. Sci.* 358, 667–674.
- Kajiwara, R., Wouterlood, F.G., Sah, A., Boekel, A.J., Baks-te Bulte, L.T., Witter, M.P., 2008. Convergence of entorhinal and CA3 inputs onto pyramidal neurons and interneurons in hippocampal area CA1—an anatomical study in the rat. *Hippocampus* 18, 266–280.
- Kandel, E., Spencer, W., Brinley, F.J., 1961. Electrophysiology of hippocampal neurons. I. Sequential invasion and synaptic organization. *J. Neurophysiol.* 24, 225–242.
- Karnup, S., Stelzer, A., 1999. Temporal overlap of excitatory and inhibitory afferent input in guinea-pig CA1 pyramidal cells. *J. Physiol.* 516 (Pt 2), 485–504.
- Kawamura, Y., Manita, S., Nakamura, T., Inoue, M., Kudo, Y., Miyakawa, H., 2004. Glutamate release increases during mossy-CA3 LTP but not during Schaffer-CA1 LTP. *Eur. J. Neurosci.* 19, 1591–1600.
- Kojima, S., Nakamura, T., Nidaira, T., Nakamura, K., Ooashi, N., Ito, E., Watase, K., Tanaka, K., Wada, K., Kudo, Y., Miyakawa, H., 1999. Optical detection of synaptically induced glutamate transport in hippocampal slices. *J. Neurosci.* 19, 2580–2588.
- Lacaille, J.C., Schwartzkroin, P.A., 1988a. Stratum lacunosum-moleculare interneurons of hippocampal CA1 region II. Intracellular and intradendritic recordings of local circuit synaptic interactions. *J. Neurosci.* 8, 1411–1424.
- Lacaille, J.C., Schwartzkroin, P.A., 1988b. Stratum lacunosum-moleculare interneurons of hippocampal CA1 region. I. Intracellular response characteristics, synaptic responses, and morphology. *J. Neurosci.* 8, 1400–1410.
- Liu, G., 2004. Local structural balance and functional interaction of excitatory and inhibitory synapses in hippocampal dendrites. *Nat. Neurosci.* 7, 373–379.
- Magee, J.C., Johnston, D., 1995. Synaptic activation of voltage-gated channels in the dendrites of hippocampal pyramidal neurons. *Science* 268, 301–304.
- Mann, E.O., Paulsen, O., 2005. Mechanisms underlying gamma (‘40 Hz’) network oscillations in the hippocampus—a mini-review. *Prog. Biophys. Mol. Biol.* 87, 67–76.
- Mann, E.O., Paulsen, O., 2006. Keeping inhibition timely. *Neuron* 49, 8–9.
- Mann, E.O., Tominaga, T., Ichikawa, M., Greenfield, S.A., 2005a. Cholinergic modulation of the spatiotemporal pattern of hippocampal activity in vitro. *Neuropharmacology* 48, 118–133.
- Mann, E.O., Suckling, J.M., Hajos, N., Greenfield, S.A., Paulsen, O., 2005b. Perisomatic feedback inhibition underlies cholinergically induced fast network oscillations in the rat hippocampus in vitro. *Neuron* 45, 105–117.
- Megias, M., Emri, Z., Freund, T.F., Gulyas, A.I., 2001. Total number and distribution of inhibitory and excitatory synapses on hippocampal CA1 pyramidal cells. *Neuroscience* 102, 527–540.
- Migliore, M., 2003. On the integration of subthreshold inputs from Perforant Path and Schaffer Collaterals in hippocampal CA1 pyramidal neurons. *J. Comput. Neurosci.* 14, 185–192.
- Migliore, M., Hoffman, D.A., Magee, J.C., Johnston, D., 1999. Role of an A-type K⁺ conductance in the back-propagation of action potentials in the dendrites of hippocampal pyramidal neurons. *J. Comput. Neurosci.* 7, 5–15.
- Mochida, H., Sato, K., Sasaki, S., Yazawa, I., Kamino, K., Momose-Sato, Y., 2001. Effects of anisomycin on LTP in the hippocampal CA1: long-term analysis using optical recording. *Neuroreport* 12, 987–991.
- Nevian, T., Larkum, M.E., Polsky, A., Schiller, J., 2007. Properties of basal dendrites of layer 5 pyramidal neurons: a direct patch-clamp recording study. *Nat. Neurosci.* 10, 206–214.
- Pouille, F., Scanziani, M., 2001. Enforcement of temporal fidelity in pyramidal cells by somatic feed-forward inhibition. *Science* 293, 1159–1163.
- Pouille, F., Scanziani, M., 2004. Routing of spike series by dynamic circuits in the hippocampus. *Nature* 429, 717–723.
- Remondes, M., Schuman, E.M., 2002. Direct cortical input modulates plasticity and spiking in CA1 pyramidal neurons. *Nature* 416, 736–740.
- Remondes, M., Schuman, E.M., 2003. Molecular mechanisms contributing to long-lasting synaptic plasticity at the temporoammonic-CA1 synapse. *Learn. Mem.* 10, 247–252.
- Ross, W.N., Salzberg, B.M., Cohen, L.B., Grinvald, A., Davila, H.V., Waggoner, A.S., Wang, C.H., 1977. Changes in absorption, fluorescence, dichroism, and birefringence in stained giant axons: optical measurement of membrane potential. *J. Membr. Biol.* 33, 141–183.
- Sayer, R.J., Redman, S.J., Andersen, P., 1989. Amplitude fluctuations in small EPSPs recorded from CA1 pyramidal cells in the guinea pig hippocampal slice. *J. Neurosci.* 9, 840–850.
- Schaefer, A.T., Angelo, K., Spors, H., Margrie, T.W., 2006. Neuronal oscillations enhance stimulus discrimination by ensuring action potential precision. *PLoS Biol.* 4, e163.
- Sjostrom, P.J., Rancz, E.A., Roth, A., Hausser, M., 2008. Dendritic excitability and synaptic plasticity. *Physiol. Rev.* 88, 769–840.
- Stuart, G.J., Dodt, H.U., Sakmann, B., 1993. Patch-clamp recordings from the soma and dendrites of neurons in brain slices using infrared video microscopy. *Pflügers Arch.* 423, 511–518.
- Tominaga, T., Tominaga, Y., Ichikawa, M., 2001. Simultaneous multi-site recordings of neural activity with an inline multi-electrode array and optical measurement in rat hippocampal slices. *Pflügers Arch.* 443, 317–322.
- Tominaga, T., Tominaga, Y., Ichikawa, M., 2002. Optical imaging of long-lasting depolarization on burst stimulation in area CA1 of rat hippocampal slices. *J. Neurophysiol.* 88, 1523–1532.
- Tominaga, T., Tominaga, Y., Yamada, H., Matsumoto, G., Ichikawa, M., 2000. Quantification of optical signals with electrophysiological signals in neural activities of Di-4-ANEPPS stained rat hippocampal slices. *J. Neurosci. Methods* 102, 11–23.
- Tominaga, Y., Ichikawa, M., Tominaga, T., 2003. Visualization of steady membrane potential change in area CA1 of rat hippocampal slices with voltage sensitive dye optical imaging. In: *Society for Neuroscience*. New Orleans, .
- Turner, D.A., 1988. Waveform and amplitude characteristics of evoked responses to dendritic stimulation of CA1 guinea-pig pyramidal cells. *J. Physiol.* 395, 419–439.
- Turner, D.A., 1990. Feed-forward inhibitory potentials and excitatory interactions in guinea-pig hippocampal pyramidal cells. *J. Physiol.* 422, 333–350.
- Verheugen, J.A., Fricker, D., Miles, R., 1999. Noninvasive measurements of the membrane potential and GABAergic action in hippocampal interneurons. *J. Neurosci.* 19, 2546–2555.

